Astronomy & Astrophysics manuscript no. 19878
January 31, 2022

The high-field polar RX J1007.5–2017

H.-C. Thomas[1⋆], K. Beuermann[2], K. Reinsch[2], A.D. Schwope[3], and V. Burwitz[4]

[1] MPI für Astrophysik, Karl-Schwarzschild-Str. 1, D-85740 Garching, Germany
[2] Institut für Astrophysik, Friedrich-Hund-Platz 1, 37077 Göttingen, Germany,
[3] Leibniz-Institut für Astrophysik Potsdam (AIP), An der Sternwarte 16, 14482 Potsdam, Germany
[4] MPI für extraterrestrische Physik, Giessenbachstr. 6, 85740 Garching, Germany

Received 25 June 2012 / Accepted 3 September 2012

ABSTRACT

We report optical and X-ray observations of the high-field polar RX J1007.5–2017 performed between 1990 and 2012. It has an orbital period of 208.60 min determined from the ellipsoidal modulation of the secondary star in an extended low state. The spectral flux of the dM3- secondary star yields a distance of 790 ± 105 pc. At low accretion levels, RX J1007.5–2017 exhibits pronounced cyclotron emission lines. The second and third harmonic fall in the optical regime and yield a field strength in the accretion spot of 94 MG. The source is highly variable on a year-to-year basis and was encountered at visual magnitudes between $V \sim 20$ and $V \sim 16$. In the intermediate state of 1992 and 2000, the soft X-ray luminosity exceeds the sum of the luminosities of the cyclotron source, the hard X-ray source, and the accretion stream by an order of magnitude. An X-ray high state, corresponding to the brightest optical level, has apparently not been observed so far.

Key words. stars: cataclysmic variables – stars: magnetic fields – stars: individual: RX J1007.5–2016 – binaries: close – X-rays: stars – accretion

1. Introduction

In polars, a subclass of cataclysmic variables (CVs), a magnetic white dwarf accretes matter from its Roche-lobe filling low-mass main-sequence companion. The strong magnetic field channels the flow onto a small accretion spot on the surface of the white dwarf, where the energy not expanded in the accretion stream is released in form of hard X-rays, soft X-rays, and cyclotron radiation. About 100 of these systems are known, most of them discovered as bright soft X-ray and EUV sources. The spectral characteristics of the spot emission depend sensitively on the magnetic field strength B in the accretion spot and on the density of the accreted matter (e.g., (e.g. Kuijpers & Pringle 1982; Fischer & Beuermann 2001). The distribution of observed field strengths in polars ranges from 10 MG to about 200 MG, with only three stars known to possess a field strength exceeding 100 MG (Schwope et al. 2009). For comparison, single magnetic white dwarfs are known to possess field strengths up to 1000 MG and display a higher incidence of very high field strengths. It is not known why such systems are lacking among the polars. Either post-common envelope binaries contain fewer white dwarfs with very high field strengths, or we fail to detect these systems once they reach the CV-stage. RX J1007.5–2017 (henceforth RXJ1007) is one of the few high-field polars. We present here a comprehensive analysis of its properties.

RXJ1007 was discovered in 1990 as a bright, very soft X-ray source in the ROSAT All Sky Survey and was subsequently identified with a 19-mag magnetic cataclysmic variable of the polar subclass (Beuermann & Thomas 1993; Thomas & Beuermann 1998; Reinsch et al. 1999). In this paper, we summarize our observations of RXJ1007 carried out over more than two decades, from its discovery in 1990 to 2012. The analysis of the early data suffered from the lack of a sufficiently accurate ephemeris, preventing a proper phasing of the data taken over the years in different wavelength regimes. This problem has now been overcome and the entire set of so-far unpublished data is presented here. Our analysis is based on optical observations, comprising time-resolved spectrophotometry, spectropolarimetry, and photometry. It includes an analysis of the ROSAT X-ray data and a re-analysis of the XMM-Newton X-ray data previously discussed by Ramsay & Cropper (2003).

⋆ Deceased 18 January 2012

2. Observations and data analysis

Table 1 contains a log of our own and previously published observations. RXJ1007 displayed substantial long-term variability both at X-ray and optical wavelengths. It was encountered in low states of accretion in 1997 and 2011/2012, in intermediate states in 1992, 2001, and 2010, and in a high state in 2000. The optical position of RXJ1007 is $\alpha_{2000} = 10^{\rm h}07^{\rm m}34\overset{\rm s}{.}6$, $\delta_{2000} = -20°17'32''$.

2.1. X-ray observations

RXJ1007 was observed from 24–26 November 1990 in the ROSAT All-Sky-Survey (RASS) with the Position Sensitive Proportional Counter (PSPC) as detector for a total of 510 s (25 sightings). The highly variable source 1RXS J100734.4-201731 had a mean count rate of 1.0 cts s^{-1} and a very soft spectrum. It was subsequently observed with the ROSAT PSPC on 17 November 1992 with a total exposure time of 10 ks and again found to be very soft with a lower mean count rate of 0.37 cts s^{-1}. Ramsay & Cropper (2003) observed the source on 7 December 2001 with XMM-Newton with the European Photon Imaging Camera (EPIC pn) for 5.5 ks. This observation showed the source in a brighter state again and confirmed the very soft X-ray spectrum.

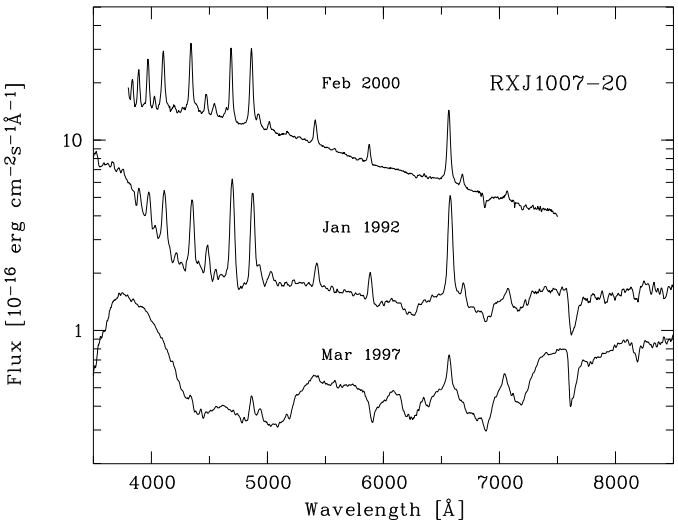

Fig. 1. Mean spectra of RXJ1007 in February 2000 (top), January 1992 (center), and March 1997 (bottom).

2.2. Optical spectrophotometry and spectropolarimetry

Phase-resolved spectrophotometry was performed in January 1992, using the ESO/MPI 2.2-m telescope with EFOSC2 and either grism G1 (FWHM resolution 50 Å) or grism G3 (FWHM resolution 10 Å). Further low-resolution spectrophotometry was performed on 6 March 1997. On 3 February 2000, when the source was at the brightest level encountered so far, we performed circular spectropolarimetry, using the ESO 3.6-m telescope with EFOSC2 and a customer-supplied quarter-wave plate. All spectrophotometry was placed on an absolute flux scale using standard stars. Fig. 1 shows the mean spectra of RXJ1007 in the 1992, 1997, and 2000 observations, which demonstrate its variability. In the 1997 low state, the red part of the spectrum is dominated by the TiO bands of the secondary star and the visual magnitude varies over the orbit between $V = 19.4 - 20.0$. The weak Balmer and the intense cyclotron emission lines indicate that low-level accretion is still taking place. The 1992 intermediate and 2000 high states are characterized by significantly increased levels of Balmer line emission and the associated continuum, but only by a moderate increase in cyclotron emission, as discussed in Sect. 3.6. In the 2000 high state, the source varied over the orbit between $V = 16$ and 17.

The profiles of the Balmer and helium emission lines in the medium-resolution spectra of 1992 and 2000 display phase-dependent asymmetries, but the narrow and broad line components, typical of polars, cannot reliably be separated. For simplicity, we measured radial velocities by fitting single Gaussians to the strong Balmer and HeIIλ4686 emission lines. Given the lack of better-resolved low-state spectra, we measured radial velocities and line fluxes also from the weak Hα emission lines as well as radial velocities from the unresolved near-infrared NaIλ8190 absorption-line doublet in the 1997 spectra. In retrospect, the phasing of the velocities suggests that the bulk of the intermediate and high-state emission originates from the magnetically confined part of the accretion stream and the low-state Balmer emission from the heated face of the secondary star.

2.3. Optical and IR photometry

We performed time-resolved relative optical photometry in 2010–2012, using the MONET/North telescope at McDonald Observatory via the MONET browser-based remote-observing interface. The data were taken with an Apogee ALTA E47+ 1k×1k CCD camera mostly in Bessel *I* (central wavelength 8000 Å) and white light (clear filter) with exposure times of 60 s. Photometry was performed relative to the comparison star USNOA 0675 10804546 (2000: RA=$10^h07^m32.87^s$, DEC=−20°15‘36.3”), which has a DENIS *I*-band magnitude of 13.14±0.03 (Fouqué et al. 2000). Combined with standard-star

Table 1. Summary of observations: X = X-ray, S = spectrophotometry, C = circular spectropolarimetry, P = photometry, WL = white light.

Date	Telescope/Instrument		Range	Resol.
24–26 Nov 1990	ROSAT / PSPC	X	0.11–2.0 keV	
9–13 Jan 1992	ESO 2.2m / EFOSC2	S	3500–9000Å	40 Å
		S	3500–5400Å	10 Å
17 Nov 1992	ROSAT / PSPC	X	0.11–2.0 keV	
15 Nov 1995	ESO 2.2m / EFOSC2	S	3800–9100Å	30 Å
6 Mar 1997	ESO 2.2m / EFOSC2	S	3500–10200Å	50 Å
14 Dec 1999	2MASS	P	J, H, K_s	
2–3 Feb 2000	ESO 3.6m / EFOSC2	C	3378–7516Å	15 Å
7 Dec 2001	XMM / EPIC pn	X	0.22–8.5 keV	
19–20 Jan 2010	MONET/N	P	$I_{Bessell}$, Sloan g	
Jan – Mar 2011	MONET/N	P	$I_{Bessell}$, WL	
2 Jan 2012	MONET/N	P	$I_{Bessell}$	

Table 2. New photometric minima with $O-C$ residuals from Eq. 1.

E	BJD(TDB) 24000000+	Error (day)	O–C (day)	Orbital Phase	Band
−45458.0	48630.7399	0.0020	0.0015	0.010	7500Å
−32460.0	50513.6773	0.0020	−0.0023	−0.016	7500Å
0.0	55215.9649	0.0020	0.0023	0.016	$I_{Bessell}$
–0.5	55215.8915	0.0020	0.0014	0.501	$I_{Bessell}$
6.0	55216.8337	0.0030	0.0020	0.014	Sloan g
2408.5	55564.8625	0.0030	−0.0048	0.467	WL
2409.0	55564.9378	0.0030	−0.0019	−0.013	WL
2415.5	55565.8790	0.0020	−0.0024	0.483	WL
2457.0	55571.8921	0.0020	−0.0011	−0.008	WL
2457.5	55571.9622	0.0020	−0.0034	0.477	WL
2484.5	55575.8754	0.0020	−0.0016	0.489	$I_{Bessell}$
2485.0	55575.9514	0.0020	0.0020	0.014	$I_{Bessell}$
2485.5	55576.0200	0.0030	−0.0019	0.487	$I_{Bessell}$
2587.5	55590.7981	0.0020	0.0002	0.501	$I_{Bessell}$
2588.0	55590.8689	0.0040	−0.0015	−0.011	$I_{Bessell}$
2588.5	55590.9487	0.0060	0.0059	0.541	$I_{Bessell}$
2594.5	55591.8151	0.0020	0.0031	0.522	WL
2595.0	55591.8857	0.0020	0.0013	0.009	WL
2642.5	55598.7691	0.0030	0.0036	0.525	$I_{Bessell}$
2643.0	55598.8402	0.0020	0.0023	0.016	$I_{Bessell}$
2643.5	55598.9086	0.0030	−0.0017	0.488	$I_{Bessell}$
2835.5	55626.7192	0.0050	−0.0050	0.466	$I_{Bessell}$
2836.0	55626.7961	0.0030	−0.0006	−0.004	$I_{Bessell}$
2843.0	55627.8101	0.0030	−0.0006	−0.004	WL
4921.5	55928.9102	0.0020	−0.0001	0.499	$I_{Bessell}$

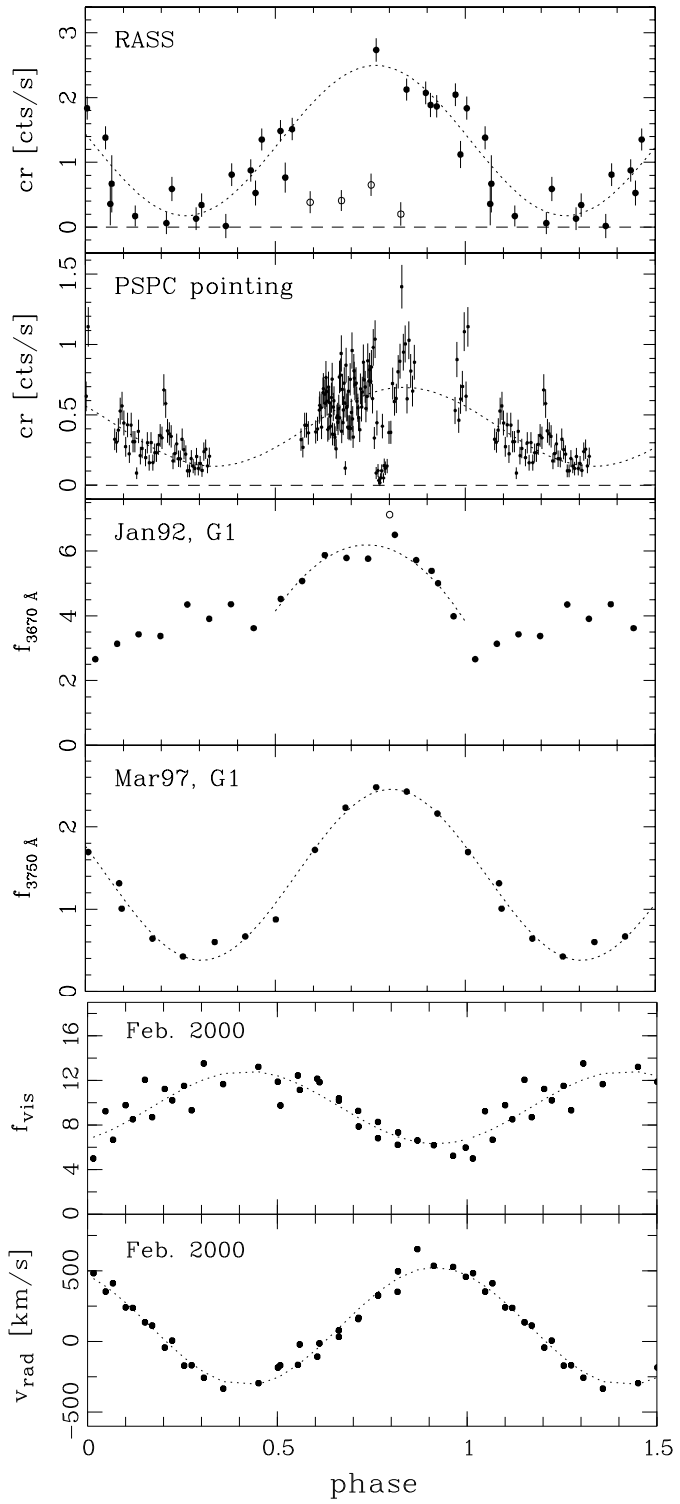

Fig. 2. Orbital variations of RXJ1007 from top: (1) 1990 X-ray light curve from the ROSAT All Sky Survey; (2) 1992 ROSAT pointed observation; (3) 1992 quasi *U*-band flux; (4) 1997 quasi *U*-band flux; (5) 2000 visual flux; (6) 2000 Balmer/HeII emission-line radial velocity. The optical fluxes are in units of 10^{-16} erg cm^{-2}s^{-1}Å^{-1}.

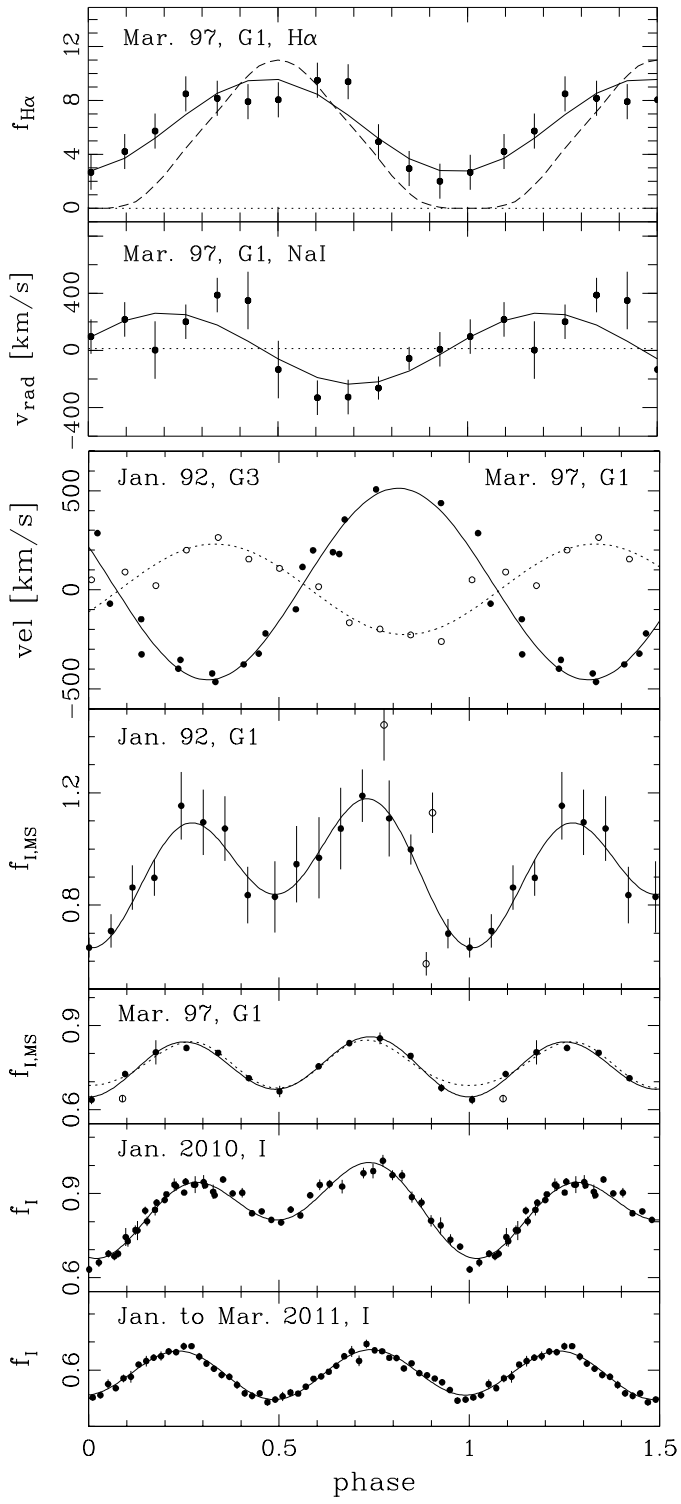

Fig. 3. Orbital variations continued: (1) 1997 Hα emission-line flux; (2) 1997 NaIλ8190 absorption-line radial velocity ; (3) 1997 Hα emission-line radial velocity (open circles, dashed curve) and 1992 Balmer/HeII emission-line radial velocity (filled circles, solid curve); (4) 1992 $f_{7500\text{Å}}$ flux; (5) 1997 $f_{7500\text{Å}}$ flux; (6) 2010 *I*-band flux; (7) 2011 *I*-band flux.

measurements in the 1992 and 1997 campaigns, we derived a common *I*-band calibration for the spectrophotometry and photometry. All our *I*-band data display a clear double-wave orbital modulation. RXJ1007 was found at $I = 17.5 - 18.1$ in January 1992, $I = 17.75$–18.08 in March 1997, $I = 17.28$–17.74 in January 2010, and $I = 17.71 - 18.08$ in January–March 2011 as well as January 2012. The source has an entry in the 2-micron All

Sky Survey (2MASS) catalog, which gives $J = 16.30 \pm 0.10$, $H = 15.63 \pm 0.12$, and $K_s = 15.22 \pm 0.13$.

3. Results

In this section, we describe first the effort to derive an accurate orbital ephemeris, which allows us to correctly phase the observations collected over more than 20 years, and then continue to discuss the physical properties of the system.

3.1. Orbital period

Early in the project, we obtained approximate values of the orbital period P of RXJ1007 by folding the X-ray fluxes (Fig. 2, panels 1 and 2 from top), the optical spectrophotometric fluxes, and the Balmer and HeII emission-line radial velocities (Fig. 2, panels 3–6, and Fig. 3 panel 3 from top, solid circles). The individual observations yielded $P = 208.1 \pm 0.7$ min (RASS), $P = 205 \pm 3$ **min** (ROSAT pointed), and $P = 208.2 \pm 0.3$ min (1992 radial velocities), suggesting $P \simeq 0.145$ d. All attempts to derive a long-term ephemeris from these data suffered from alias problems.

An alternative approach is suggested by the quasi-I band fluxes in Fig. 3 (panels 4 and 5 from top), which show what may be the ellipsoidal modulation of the secondary star in the 1992 intermediate and the 1997 low-state data. The two light curves refer to the 7450–7550 Å band, which measures the flux of the secondary star with some contribution from the white dwarf and the accretion stream. These early data were supplemented by the I-band light curves taken in the 2010 intermediate and the 2011–2012 extended low states (Fig. 3, bottom two panels). For the dM3– secondary star in RXJ1007 (Sect. 3.3), the spectral flux at 7500 Å and the mean Bessell I-band flux agree within a few percent (Beuermann 2006), allowing an easy comparison. The four light curves shown have a common ordinate scale normalized to the peak flux in 2010, which corresponds to $I = 17.3$. Standard theory of the ellipsoidal modulation for Roche-lobe filling stars predicts two minima, of which the deeper one, according to von Zeipel's (1924) law, occurs at superior conjunction of the secondary star. This order may be reversed if the low-gravity hemisphere of the secondary is radiatively heated by the accreting white dwarf. The different fluxes in the displayed light curves cannot be explained by heating alone, however, and the presence of an accretion-induced component is indicated for at least the 1992 and 2010 intermediate states.

In a first step toward an ephemeris, we corrected the observed minimum times in 1992, 1997, and 2010 for this additional light source. We performed Fourier fits to the light curves, using two sinusoids with periods $P/2$ and P. The former approximates the ellipsoidal light curve (assuming two equal minima) and the latter represents the additional light source. The fit has five free parameters, the period P, the two amplitudes, and two phase shifts. Higher harmonics are not needed for the present purpose. The resulting fits are shown as solid lines in Fig. 3 (bottom four panels) and an example of the $P/2$ sinusoid is added as a dotted curve in the third panel from the bottom. We used these fits for the sole purpose of correcting the observed minimum times to those that the $P/2$ component alone would have had. In the low state, this correction practically vanishes. Table 2 lists the minimum times with this small correction included. In a second step, we performed a period search around P/2, using the times of Table 2. The best-fit period is $P/2 = 0.072431961(18)$ d with $\chi^2 = 22.2$ for 23 degrees of freedom (d.o.f.). The next-best alias corresponds to a difference of one cycle on the $P/2$ scale over one year. It has an unacceptable $\chi^2 = 58.0$ and can be excluded. Hence, our fit fixes the orbital period P, but still leaves us with the choice of which of the two minima corresponds to inferior conjunction of the secondary. It is encouraging though that the deeper minima in 1992 and 2010 are separated by an even number of $P/2$ cycles and thus occur at the same orbital phase. We adopt the deeper minimum in the intermediate states as corresponding to inferior conjunction, a choice that we justify in Sect. 3.2.2, and obtain the ephemeris

$$T_0 = \mathrm{BJD(TDB)}\ 24\,55215.96256(48) + 0.144\,863\,923\,(36)\,E, \quad (1)$$

where T_0 refers to the inferior conjunction of the secondary star. All orbital phases quoted in this paper refer to Eq. 1.

3.2. Orbital variations

Figures 2 and 3 display the X-ray fluxes, optical fluxes, and radial velocities folded over the orbital period. We determined the times of maximum flux or of maximum positive radial velocity by fitting sinusoids to the data, which are shown in the as dotted or solid curves in the appropriate panels. All time tags from the optical telescopes and from the ROSAT satellite are given in UTC, while XMM Newton has the leap seconds added and provides times in Terrestrial Time (TT). We converted all times to Barycentric Dynamical Time (TDB), which agrees with TT at the ms level[1], and corrected them for the light travel time to the solar system barycenter, i.e., we use Barycentric Julian Days in TDB or BJD(TDB). The conversion from UTC was made with the interactive tool `astroutils`[2]. Note that we quote Julian days and not modified Julian days.

3.2.1. X-ray flux

The ROSAT X-ray light curves display an orbital maximum near phase $\phi \simeq 0.78$. A pronounced dip in the light curve of the pointed ROSAT observation (Fig. 2, second panel from top) occurs just before maximum, which lasts from $\phi = 0.73$ to 0.78 and is likely produced by the accretion stream crossing the line of sight. Ramsay & Cropper (2003) observed RXJ1007 with the CCD cameras on board of XMM-Newton for part of the orbital period at unknown phase. With the ephemeris of Eq. 1, we now find that their observation intervals covered orbital phases $\phi = 0.13 - 0.71$ (EPIC MOS) and $\phi = 0.31 - 0.69$ (EPIC pn), just missing the dip. The ROSAT light curves show X-ray emission at all orbital phases, suggesting either that the X-ray emitting spot never disappears completely behind the horizon, or that we are seeing emission from more than one region on the white dwarf. The X-ray flux varies substantially on time scales down to minutes. Orbit-to-orbit variability is responsible for the low fluxes in the RASS light curve (Fig. 2, top panel, open circles).

3.2.2. Radial velocities in the intermediate and high states

Peak radial velocity of the Balmer and HeIIλ4686 line emission in the 1992 and 2000 intermediate and high states occur at orbital phases near X-ray maximum, suggesting that the line emission originates in the magnetically confined section of the accretion stream that leads from the stagnation point in the magnetosphere to the hot spot on the white dwarf (e.g. Schwope et al. 2000;

[1] http://www.cv.nrao.edu/~rfisher/Ephemerides/times.html
[2] http://astroutils.astronomy.ohio-state.edu/time/

Staude et al. 2001). The large mean radial-velocity amplitudes of the the Hβ, Hγ, Hδ, Hϵ, and He II λ 4686 emission lines, $K = 484 \pm 30$ km s^{-1} in 1992 and and $K = 470 \pm 30$ km s^{-1} in 2000, support this notion. At this point, it is appropriate to comment on the phase convention adopted in Section 3.1. Had we assigned $\phi = 0$ to the less deep I-band minimum, we would face the implausible situation that the radial velocity maxima would occur half an orbit offset from the X-ray maxima. Furthermore, the coincidence of maximum X-ray and 1992 and 1997 cyclotron fluxes would be destroyed.

3.2.3. Optical-continuum fluxes

The quasi-U band fluxes in the center two panels of Fig. 2 represent the cyclotron flux in the third harmonic, with a small contribution from the white dwarf in 1997 and an additional larger contribution from the accretion stream in 1992. Peak flux agrees in phase with the X-ray maximum and the radial velocity maximum in 1992, and approximately also in 2000. We note that cyclotron beaming, which shapes the optical light curves in many polars, is not prominent for the low harmonics observed in RXJ1007. The quasi-V band flux $f_{\rm vis}$ observed in 2000 displays an entirely different behavior, being in antiphase to the emission line radial velocities $v_{\rm rad}$ (bottom panels of Fig. 2). The high-state continuum flux must, therefore, have an origin different from the low- and intermediate-state cyclotron fluxes. A straightforward interpretation assigns the emission to the accretion stream as the dominant light source in the high state. The excess flux of the 2MASS data over the infrared continuum of the secondary star would then represent the Brackett and Pfund continua emitted in an intermediate or high state. The observed phase shift between $f_{\rm vis}$ and $v_{\rm rad}$ in 2000 can be understood if the free-free and recombination continuum of the stream is optically thick and its brightest inner section is hidden from view at the phase of maximum recessional velocity. This model implies that cyclotron emission is not a major contributor to the optical flux in the high state. Cyclotron line emission, while the dominant source of the low-state U-band flux, is restricted to the optically thin fringes of the accretion spot in the high state and possibly shows little variation between the low and high states. This behavior is expected if high-density accreted matter carries its energy into subsphotospheric layers instead of expanding it in free-standing shocks above the photosphere of the white dwarf (e.g. Kuijpers & Pringle 1982; Fischer & Beuermann 2001).

Table 3. Times and phases of events around the orbit

Maximum of	BJD(TDB) 24000000+	ϕ
X-ray flux RASS 1990	48220.1588 (40)	0.76(3)
X-ray flux ROSAT 1992	48943.6190 (40)	0.83(3)
Hβ–Hϵ, HeII radial velocity 1992	48631.7244 (40)	0.81(3)
Hβ–Hγ, HeII radial velocity 2000	51577.6920 (50)	0.91(4)
Visual flux 2000	51577.6197 (50)	0.41(4)
NaI radial velocity 1997	50513.7086 (70)	0.20(5)
Hα radial velocity 1997	50513.7260 (70)	0.32(5)
Hα line flux 1997	50513.7477 (70)	0.47(5)
Cyclotron flux 3670Å 1992	48630.6984 (40)	0.73(3)
Cyclotron flux 3750Å 1997	50513.6496 (30)	0.79(2)

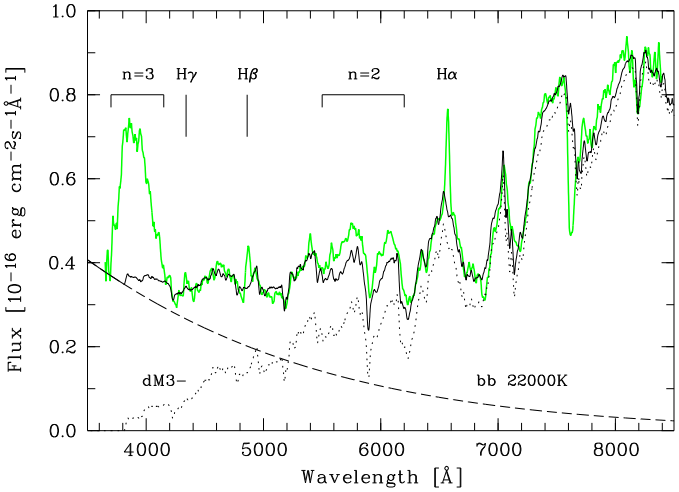

Fig. 4. Observed spectrum in the 1997 low state at cyclotron minimum (green curve), fitted by a dM3- star and a blackbody (see text).

3.2.4. Radial velocities and Hα line flux in the low state

The top three panels in Fig. 3 display the Hα line flux in arbitrary units, the NaIλ8190 radial velocity, and the Hα radial velocity (open circles), as measured from the 1997 low-resolution spectra. The line flux peaks at $\phi = 0.5$, when the irradiated face of the secondary is in view, and maximum recessional radial velocity occurs at $\phi \simeq 0.25$, suggesting that these quantities trace the motion of the secondary, providing additional support for our phase convention. Heating does occur, as indicated by the fact that the NaI line is best defined when the back side is in view. However, the Hα flux does not drop to zero at $\phi = 0$, as expected for an origin on the heated side of the secondary and illustrated by the dashed curve calculated for an inclination $i = 73°$ (Sect. 3.6). Higher resolved spectra are needed to resolve the origin of the low-state Hα emission. The measured radial-velocity amplitudes are $K'_{2,{\rm H}\alpha} = 218 \pm 30$ km s^{-1} and $K'_{2,{\rm NaI}} = 278 \pm 30$ km s^{-1}. The true radial velocity amplitude K_2 of the secondary is probably larger than the former value and smaller than the latter, and we compromise on $K_2 \simeq 250 \pm 20$ km s^{-1}.

3.3. The secondary star

TiO features of the secondary star dominate the 1997 low-state spectra longward of 6200 Å. The secondary star is best detected at orbital minimum of the cyclotron flux near $\phi = 0.25$, which corresponds to the maximum of the ellipsoidal modulation. The mean of the three spectra at $\phi = 0.18$, 0.26, and 0.34 (Fig. 4, green curve) shows the M star, the blue continuum of the white dwarf, and remnant cyclotron emission in the restricted intervals of 3700–4200 Å (third harmonic) and 5500-6200 Å (second harmonic). We fitted the observed spectrum in the intervals free of cyclotron emission, using representative spectra of M2 to M4 dwarfs from the Sloan Digital Sky Survey (Rebassa-Mansergas et al. 2012) and a blackbody for the white dwarf. We find a spectral type dM3– with an uncertainty of half a spectral class (dotted black curve) and a blackbody temperature of 22000 K (dashed black curve) for a white dwarf of 0.8 $M_\odot$ with a radius of 7.4×10^8 cm at a distance of 790 pc (Sections 3.4 and 3.5). Extinction with $A_{\rm I} \sim 0.04$, as suggested by the interstellar absorbing hydrogen column density derived from the X-ray spectral fits (Section 3.7), implies an I-band flux higher by 4%.

The 7500 Å spectral flux of the secondary reduced to the level of the primary minimum at $\phi = 0$ (Fig. 3, third panel from bottom) then is $f_{7500} = 6.6 \times 10^{-17}$ erg cm^{-2}s^{-1}Å^{-1} with an error of 10% based on the uncertainties in the flux calibration. Differential extinction would lead to a minimally earlier spectral type than adopted above. This value of f_{7500} is used in Sect. 3.5 to derive the distance of RXJ1007.

The amplitude of the ellipsoidal modulation is 25% of the peak flux, a number typical of a dM star viewed at high inclination i. For a dM3– star and $i = 73°$ (Sect. 3.6), the observed modulation amplitude is reproduced using the appropriate gravity-darkening coefficient $\beta_1 = 0.65$ and limb-darkening coefficient $u_l = 0.216$ from Claret (2000a,b). The ellipsoidal modulation is also seen in the wavelength interval $\lambda = 4400$–5200 Å, where the secondary still contributes about half of the observed flux.

3.4. Masses of the stellar components of RXJ1007

The mean Roche-lobe radius of the secondary star is given by

$$R_2/R_\odot = 0.234\,(M_2/M_\odot)^{1/3}\,P^{2/3}\,f, \qquad (2)$$

where M_2 is its mass, P is the orbital period in hours, and $f \simeq 0.989$ (Kopal 1959). In CVs above the period gap, mass loss has usually driven the secondary somewhat out of thermal equilibrium (Knigge et al. 2011). As a consequence, its radius is increased beyond that of an undisturbed field star by a higher percentage than expected from tidal and centrifugal forces alone (Kippenhahn & Thomas 1970; Renvoizé et al. 2002). Depending on the long-term average of the mass transfer rate $\dot{M}$, the secondary could have a mass as large as 0.40 $M_\odot$ with a spectral type dM2.9 or as low as 0.24 $M_\odot$with a spectral type dM3.9 (Knigge et al. 2011, their Table 2). The observed spectral type of dM3- favors a larger mass and settle on $M_2 = 0.35 \pm 0.05$, which allows for moderate bloating. From Eq. 2, we obtain $R_2 = (2.60 \pm 0.13)\,10^{10}$ cm. An estimate of the primary mass M_1 can be obtained from the radial-velocity amplitude K_2 derived in Section 3.2.4. With $i = 73°$, we obtain $M_1 = 0.80 \pm 0.15\,M_\odot$.

3.5. The distance of RXJ1007

We obtained the distance of RXJ1007 from the observed spectral flux of the secondary star combined with its radius and surface brightness. Roche geometry yields an effective radius of the projected cross section of the star at $\phi = 0$ and $i = 73°$ of $R_{\rm proj} = 0.957\,R_2 = 2.49 \times 10^{10}$ cm. With the 7500 Å spectral flux of the secondary star from above, $f_{7500} = (6.6 \pm 0.7) \times 10^{-17}$ erg cm^{-2}s^{-1}Å^{-1}, and the surface brightness of a dM3– star at 7500 Å of $F_{7500} = (6.4 \pm 0.9) \times 10^5$ erg cm^{-2}s^{-1}Å^{-1} (Beuermann 2006), the distance is obtained as $d = R_{\rm proj}\,(F_{7500}/f_{7500})^{1/2} = (2.45 \pm 0.32) \times 10^{21}$ cm $= 790 \pm 105$ pc.

3.6. Cyclotron spectroscopy

Cyclotron line emission dominates the 1997 low-state spectra and displays a marked orbital variation with a minimum at $\phi \simeq 0.3$ and a maximum at $\phi \simeq 0.8$. The latter coincides with the X-ray maximum (Fig. 2). Peak flux occurs when the line of sight is closest to the axis of the accretion funnel. This differs from the situation encountered in low-field polars, where cyclotron beaming results in a flux minimum in the direction of the funnel. In RXJ1007, however, we observed in low harmonics with little or no preference of emission perpendicular to the field (note that the first harmonic is emitted primarily along the field).

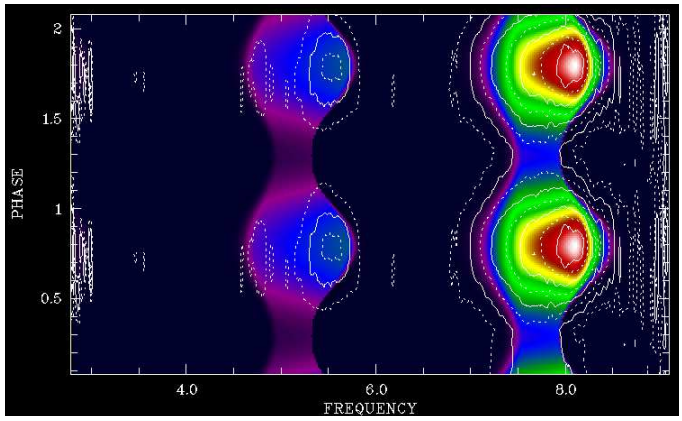

Fig. 5. 2-D representation of the phase-dependent observed and calculated cyclotron lines of RXJ1007 in 1997. The best-fit calculated spectral flux (color) is compared with the observed fluxes (contour lines). The abscissa is frequency in units of 10^{14} Hz, the ordinate is phase and data and model are displayed twice. The image shows the second and third harmonic with an indication of the first harmonic at the lowest frequencies.

The phase-resolved cyclotron spectra were obtained by subtracting the contributions of the secondary and primary star from the 13 observed spectra of the 1997 data set. At peak flux, the second and third harmonics extend over the wavelength intervals 5200–6700 Å and 3500–4400 Å, respectively. Between these intervals, the cyclotron flux is effectively zero. For a more detailed analysis, we rebinned the spectra to the spectral resolution of 50 Å and assigned 'errors' to the individual spectral bins that reflect the scatter of the original data points within each 50 Å bins. These spectra are displayed on a frequency scale in the 2-D image of Fig. 5 (contour lines). As an example, a single spectrum at maximum cyclotron flux is shown in Fig. 6 (top panel, green curve).

We fitted the entire set of cyclotron spectra simultaneously, using model spectra calculated for an isothermal homogeneous plasma slab (Barret & Chanmugam 1985, so-called constant-Λ model). The free parameters of the multi-parameter fit were the magnetic field strength B, the plasma temperature T, the dimensionless slab thickness Λ, the solid angle Ω subtended by the accretion spot as seen from the Earth, the inclination i of the system, and the direction of the accreting field line given by the polar angle β and the the azimuth ψ. The location of the spot is assumed to agree with the foot-point of the field line. We found that a consistent set of parameters exists that simultaneously fits the thirteen spectra with 50 data points each. A color

Table 4. Best-fit parameters for the fit shown in Figs. 5 and 6.

Parameter	Value	Error
Magnetic field strength (MG)	94.0	0.3
Plasma temperature (keV))	2.1	0.3
Size Parameter Λ (10^4)	2.8	+2.3,–1.3
Solid angle Ω (10^{-26} sr)	3.0	0.3
Inclination i (°)	73	1
Colatitude of field/spot β (°)	12.3	1.6
Azimuth of field/spot ψ (°)	70	4

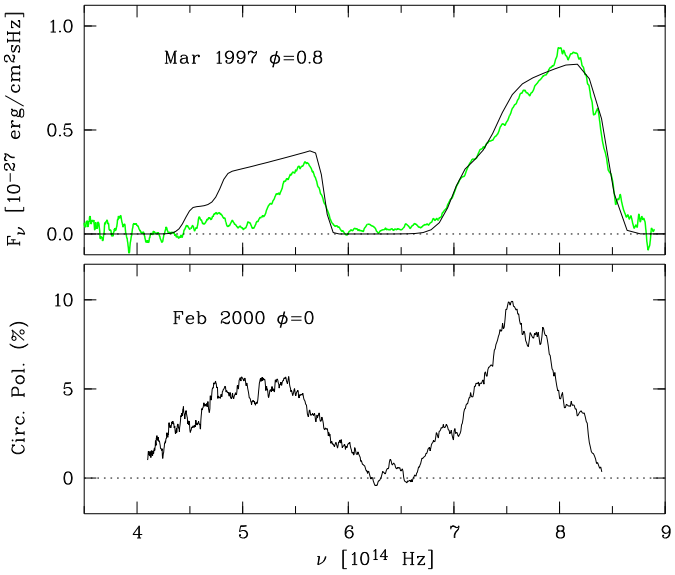

Fig. 6. Representative cyclotron spectra showing the second and third harmonic in a field of 94 MG. *Top:* Cyclotron spectrum at $\phi = 0.8$ in the 1997 low state (green) and theoretical cyclotron spectrum (black) obtained from a simultaneous fit to the entire set of spectra as shown in Fig. 5. *Bottom:* Circular polarization in the high state on 6/7 February 2000 measured around the flux minimum at orbital phase $\phi = 0$.

representation of the calculated spectral flux is shown in Fig. 5. The spectra represent the second and third harmonics in a field of 94 MG. The complete set of fitted parameters is provided in Table 4 along with their 1–σ errors. The fit has a $\chi^2 = 517$ for 643 d.o.f. It is remarkable that a close-to-perfect fit to the observed data set is possible using the fairly simple theoretical model. The fit fixes the orbital inclination of RXJ1007 at $i = 73° \pm 1°$ (1–σ error), implying that the system just escapes eclipse of the white dwarf by the secondary star. With 2.1 keV, the plasma temperature is lower than the mean temperature of 6 keV derived from the fit to the XMM spectrum, but both temperatures are substantially lower than expected for a free-standing shock on a white dwarf of 0.8 $M_\odot$.

The dominance of emission from the magnetic pole with $B = 94$ MG persists from the low state into the high state of RXJ1007. Even against the intense Paschen continuum of the 2000 high state, the second and third harmonics stand out in the circular polarization at practically the same wavelengths as in the low state (Fig. 6, bottom panel). The line shape, furthermore, suggests a low temperature similar to the 2 keV of the low state, consistent with emission from the low-density fringes of the accretion spot, in which cyclotron emission is the prime cooling agent (Woelk & Beuermann 1996, Fischer & Beuermann 2001). Radiation-hydrodynamic calculations suggest that columns with different temperatures and plasma densities may coexist in the spot and that cyclotron cooling dominates in low-density columns, in which the plasma cools before the ion and electron temperatures can equilibrate (Woelk & Beuermann 1996, Fischer & Beuermann 2001).

Despite the generally excellent agreement, some differences between the observed and calculated line profiles are noteworthy. An observed feature that is not present in the blackbody-limited line flux is the pronounced central depression in the second harmonic around 6000 Å. It is likely that this depression represents the Fraunhofer-type absorption produced by the temperature stratification in columns that are optically thick in the emitted cyclotron harmonics (Woelk & Beuermann 1996). A similar profile was observed in the cyclotron lines of the high-field polar UZ For (Rousseau et al. 1996) and was successfully modeled with the theory of Woelk & Beuermann (1996). The slight notch in the long-wavelength fall-off of the model profiles results from differences in the line profiles for the ordinary and extraordinary rays in this fairly simple theory.

3.7. The X-ray spectrum

We have re-analyzed the mean X-ray spectrum taken with XMM-Newton on 7 December 2001 (Ramsay & Cropper 2003, their Fig. 8), using an improved spectral representation of the soft and hard X-ray components. As demonstrated for AM Her (Beuermann et al. 2012), a model including two or more blackbody components may yield a more realistic estimate of the soft X-ray luminosity than the single-blackbody assumption employed by Ramsay & Cropper (2003). Our fit involves two blackbodies with best-fit temperatures $kT_1 = 59 \pm 3$ eV and $kT_1 = 32 \pm 5$ eV for a best-fit absorbing column density $N_H = 1.9 \times 10^{20}$ H-atoms cm^{-2}. The hard X-ray component was modeled with two MEKAL spectra for solar abundances and temperatures $kT = 6.0$ keV (fixed) and $kT = 0.19 \pm 0.01$) keV. The fit has a $\chi^2 = 115$ for 107 d.o.f. ($\chi^2_\nu = 1.07$). The integrated fluxes for the best-fit parameters are 3.5×10^{-11} erg cm^{-2}s^{-1} and 8.5×10^{-13} erg cm^{-2}s^{-1} for the two blackbodies and 3.5×10^{-13} erg cm^{-2}s^{-1} and 8.5×10^{-13} erg cm^{-2}s^{-1} for the two thermal components, respectively. Guided by the case of AM Her (Christian 2000), we considered that the hard X-ray component of RXJ1007 possibly contains highly absorbed components that are not accounted for by the XMM spectral fit at $E < 8$keV. We estimated that this could contribute another $(1-2) \times 10^{-13}$ erg cm^{-2}s^{-1}. Since the presence of a substantial hard X-ray component is uncertain, it is entered in Table 5 with a question mark. We caution, furthermore, that the correlated errors between the blackbody temperature and the interstellar absorbing column imply large uncertainties, preventing us from quoting errors for the fluxes. Despite all the uncertainties, however, the emission of RXJ1007 is clearly dominated by soft X-rays. In the 1992 pointed ROSAT observation, the source was fainter by almost an order of magnitude. The fit parameters are less well-defined than those of the XMM fit and are not quoted here.

Table 5. Bolometric fluxes and luminosities of RXJ1007 for the intermediate states of 1992/2001. See text for the geometry factors $\eta\pi$.

Component		F (erg cm^{-2}s^{-1})	$\eta\pi$	L (erg s^{-1})
Soft X-ray blackbody,	32 eV	8.5×10^{-11}	2π	3.2×10^{33}
	59 eV	3.5×10^{-11}	2π	1.3×10^{33}
Thermal X-rays	0.2 keV	9.0×10^{-13}	4π	6.7×10^{31}
	6.0 keV	2.8×10^{-13}	4π	2.1×10^{31}
	> 10 keV ?	1.5×10^{-13}	4π	1.1×10^{31}
Cyclotron + accretion stream		4.0×10^{-12}	4π	3.0×10^{32}
Total				4.9×10^{33}

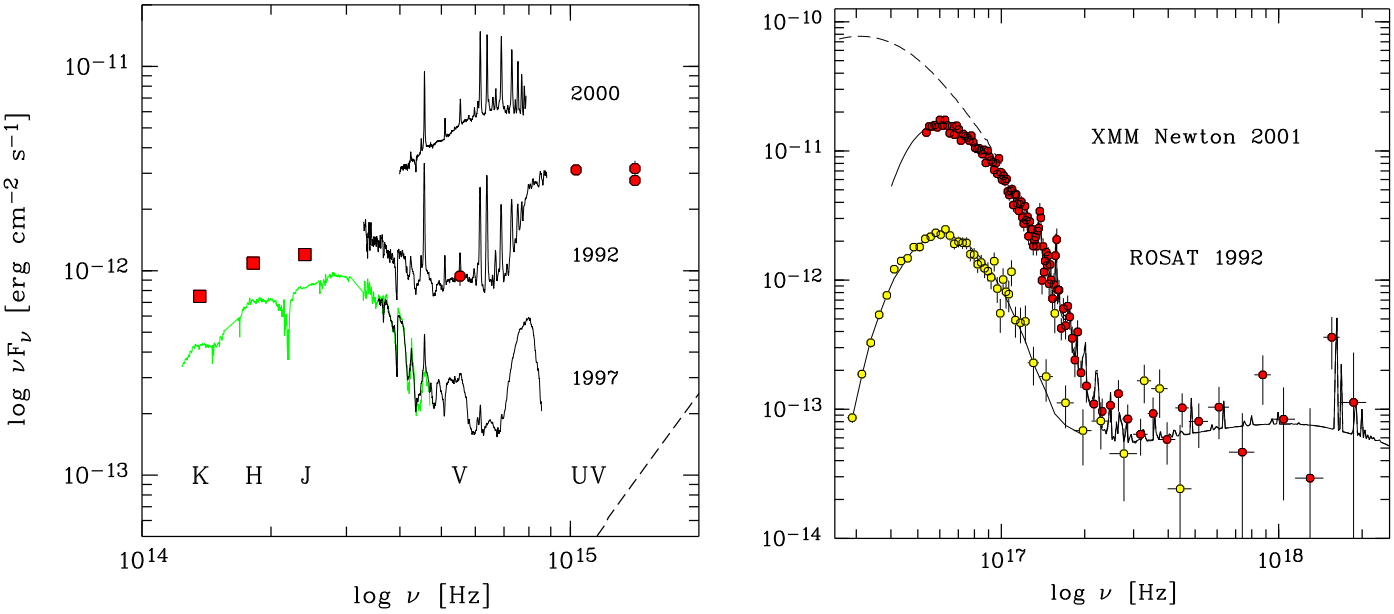

Fig. 7. Spectral energy distribution of RXJ1007-20. *Left:* IR-optical-UV part. *Right:* X-ray part. See text for further explanation.

3.8. Overall spectral energy distribution

Fig. 7 shows the spectral fluxes from the infrared to the hard X-ray regime collected into a single overall spectral energy distribution (SED). For the chosen form νf_ν vs. ν, the integrated energy flux of a component with spectral flux f_ν is $F = \int \nu f_\nu \, \mathrm{d}\log\nu$, with log the natural logarithm. Given the flux of a spectral component, the luminosity $L = \eta\pi d^2 F$ was calculated with $d = 790$ pc and the geometry factor η quoted in Table 5. As for the prototype polar AM Her (Beuermann et al. 2012), we adopted emission of the soft X-ray blackbody and of cyclotron radiation into $2\,\pi$ and of the accretion stream and the hard X-rays into $4\,\pi$.

The left panel shows our spectrophotometry of 1992, 1997, and 2000 (black curves), supplemented by the 2MASS J, H, and K-band fluxes of 1999 (red filled squares) and the visual and ultraviolet fluxes measured with the optical monitor on board of XMM-Newton simultaneous to the 2001 X-ray observation (red filled circles). For the low state, which is dominated by the secondary star, we added the flux distribution of the dM3 star LHS58 (Leggett et al. 1996, green curve) adjusted to the 1997 low-state spectrophotometry. The right panel shows the incident spectra for the 2001 XMM pn observation (red filled circles) and the 1992 ROSAT PSPC observation (open circles). For the XMM spectrum, we also included the 'source spectrum' corrected for interstellar absorption, using the X-ray spectral parameters quoted above (dashed curve in the left and the right panel).

There is a close agreement between our 1992 spectrophotometry and the 2001 XMM optical-monitor fluxes in the visual and ultraviolet bands, suggesting that they delineate the common SED of an intermediate state of accretion assumed by RXJ1007in 1992 and 2001. This SED is well documented from the infrared to the hard X-ray regime. About 92% of the bolometric flux in this state is emitted as soft X-rays, 6% as cyclotron radiation and stream emission, largely in the ultraviolet, and only 2% as hard X-rays. The dominance of soft X-rays implies that most of the accretion energy is released in shocks, which are buried in the photosphere of the white in a scenario first described by Kuijpers & Pringle (1982). The luminosity ratio $L_{\rm softX}/(L_{\rm cyc} + L_{\rm hardX} + L_{\rm stream}) \sim 11$. The low-level cyclotron emission in 1997 suggests that the associated X-ray flux was low as well. Similarly, we can only speculate that the optical high state in February 2000 was accompanied by a correspondingly increased soft X-ray flux. The rough equality of the ROSAT and XMM X-ray fluxes in the 1-2 keV range hints at a lower variability of the hard X-ray fluxes, consistent with the notion of Kuijpers & Pringle (1982) that an increased $\dot{M}$ arises primarily from dense blobs, which penetrate to subphotospheric layers.

For a white dwarf with $M_1 = 0.8\,M_\odot$ and $R_1 = 7.4 \times 10^8$ cm, the accretion luminosity in the 1992/2001 intermediate state of $L_{\rm acc} \simeq 4.9 \times 10^{33}\,\mathrm{erg\,cm^{-2}s^{-1}}$ requires an accretion rate $\dot{M} = R_1\,L_{\rm acc}/(G\,M_1) \simeq 3.4 \times 10^{16}\,\mathrm{g\,s^{-1}}$ or $5.4 \times 10^{-10}\,M_\odot\,\mathrm{yr^{-1}}$. The lack of X-ray coverage prevents an estimate of the accretion rate in a high state, but if it follows the optical continuum, it could exceed $10^{-9}\,M_\odot\,\mathrm{yr^{-1}}$ and, thereby, reach into the realm typical of long-period CVs (Knigge et al. 2011).

4. Conclusions

We have presented a comprehensive study of the high-field polar RXJ1007, which includes observations performed over more than 20 years. It is a highly variable source that was encountered at optical flux levels differing by 4 mag over the years. In the intermediate state of 1992 and 2001, RXJ1007 has a soft X-ray luminosity $L_{\rm softX} \gtrsim 0.90\,L_{\rm acc} \simeq 1.2\,L_\odot$. In a high state of accretion, the soft X-ray luminosity is possibly higher still, both relatively and absolutely. With a polar field strength of 94 MG, RXJ1007 belongs to the few high-field polars. The main accreting pole is permanently in view and is the source of the cyclotron lines observed at all accretion levels. The observed cyclotron line profiles and the low temperature in the emission region are perfectly consistent with cyclotron theory.

Acknowledgements. A draft of this paper was left by the late Hans-Christoph Thomas, who had finished analysis of the photometric MONET/N data of RXJ1007 collected in early January 2012, before he suddenly died of heart failure on 18 January 2012, aged 75. Hans-Christoph Thomas was highly regarded as a collaborator and as a friend by many colleagues in the communities dealing with stellar structure theory and with close binaries. Being one of the earliest collaborators of Rudolf Kippenhahn, Hans-Christoph Thomas was the first to

follow the evolution of a solar-like star numerically through the helium flash. Many young scientists benefitted from his ever selfless and friendly cooperation.

This work is based in part on data obtained with the MOnitoring NEtwork of Telescopes (MONET), funded by the Alfried Krupp von Bohlen und Halbach Foundation, Essen, and operated by the Georg-August-Universität Göttingen, the McDonald Observatory of the University of Texas at Austin, and the South African Astronomical Observatory. The spectroscopic observations were obtained with the ESO 3.6-m telescope under Program No. 64.H-0311(A) and with the ESO/MPI 2.2-m telescope in MPI time. This paper makes use of observations with the X-ray telescopes on board of the German/British/American ROSAT satellite and XMM-Newton, an ESA Science mission with instruments and contributions directly funded by ESA Member States and NASA.

References

Baraffe I., Chabrier G., Allard F., Hauschild P.H., 1998, A&A 337, 403
Barrett P.E., Chanmugam G., 1985, ApJ 298, 743
Beuermann, K. 2006, A&A, 460, 783
Beuermann, K., Burwitz, V., & Reinsch, K. 2012, A&A, 543, A41
Beuermann K., Thomas H.-C., 1990, A&A 230, 326
Beuermann K., Thomas H.-C., 1993, Adv. Space Res. 13 (12), 115
Christian, D. J. 2000, AJ, 119, 1930
Claret A., 2000, A&A 359, 289
Claret A., 2000, A&A 363, 1081
Fischer, A., & Beuermann, K. 2001, A&A, 373, 211
Fouqué, P., Chevallier, L., Cohen, M., et al. 2000, A&AS, 141, 313
Kippenhahn, R., & Thomas, H.-C. 1970, IAU Colloq. 4: Stellar Rotation, 20
Knigge, C., Baraffe, I., & Patterson, J. 2011, ApJS, 194, 28
Kuijpers, J., & Pringle, J. E. 1982, A&A, 114, L4
Leggett, S. K., Allard, F., Berriman, G., Dahn, C. C., & Hauschildt, P. H. 1996, ApJS, 104, 117
Ramsay, G., & Cropper, M. 2003, MNRAS, 338, 219
Rebassa-Mansergas, A., Nebot Gómez-Morán, A., Schreiber, M. R., et al. 2012, MNRAS, 419, 806
Reinsch, K., Burwitz, V., Beuermann, K., & Thomas, H.-C. 1999, Annapolis Workshop on Magnetic Cataclysmic Variables, 157, 187
Renvoizé, V., Baraffe, I., Kolb, U., & Ritter, H. 2002, A&A, 389, 485
Rousseau, T., Fischer, A., Beuermann, K., & Woelk, U. 1996, A&A, 310, 526
Schwarz, R., Reinsch, K., Beuermann, K., & Burwitz, V. 2005, A&A, 442, 271
Schwope, A. D., Catalán, M. S., Beuermann, K., et al. 2000, MNRAS, 313, 533
Schwope, A. D., Nebot Gomez-Moran, A., Schreiber, M. R., Gänsicke, B. T. 2009, A&A, 500, 867
Staude, A., Schwope, A. D., & Schwarz, R. 2001, A&A, 374, 588
Thomas H.-C., Beuermann K., Reinsch K., et al., 1998, A&A 335, 467
von Zeipel, H., 1924, Mon. Not. Roy. Astron. Soc. 84, 665
Woelk, U., & Beuermann, K. 1996, A&A, 306, 232